Macromolecular Research

Article

DOI 10.1007/s13233-022-0067-z

www.springer.com/13233 pISSN 1598-5032 eISSN 2092-7673

Corrosion-Resistant Polyaniline-Coated Zinc Tungstate Nanocomposites with Enhanced Electric Properties for Electromagnetic Shielding Applications

Abdul Kadar C. H[1,2,3]
Muhammad Faisal*[,1,2]
N. Maruthi*[,1,2,4]
Narasimha Raghavendra*[,5]
B. P. Prasanna[4]
S. R. Manohara[6]

[1] Research Center-Physics, Department of Science and Humanities, PES University-Electronic City Campus, Bengaluru 560100, Karnataka, India
[2] Research Center-Physics, PES Institute of Technology-Bangalore South Campus, Affiliated to Visvesvaraya Technological University, Belagavi 590018, Karnataka, India
[3] Department of Physics, The Oxford College of Engineering, Bommanahalli, Bengaluru 560068, India
[4] Department of Physics, Faculty of Engineering and Technology, Jain University, Bengaluru 562112, India
[5] Department of Chemistry, K.L.E Societies P.C. Jabin Science College, Hubballi 580031, India
[6] Nano-Composites and Materials Research Lab, Department of Physics, Siddaganga Institute of Technology, Tumakuru 572103, India

Received December 9, 2021 / Revised March 23, 2022 / Accepted April 19, 2022

Abstract: This paper presents the suitability of polyaniline/zinc tungstate (PANI/$ZnWO_4$) nanocomposites with tunable electrical properties for a range of multifunctional applications. *In-situ* oxidative polymerization method was employed to synthesize the PANI/$ZnWO_4$ nanocomposites with different mass percentages of the dispersant $ZnWO_4$ (10%, 20%, 30%, and 40%). The structural features of the samples were analyzed using X-ray diffraction, Fourier transform infrared spectroscopy, scanning electron microscopy (SEM), transmission electron microscopy, and Raman spectroscopy techniques. Frequency-dependent electrical conductivity studies and dielectric responses were investigated for PANI/$ZnWO_4$ nanocomposites in the range of 100 Hz - 1 MHz. PANI/$ZnWO_4$ nanocomposites showed tunability in the observed high dielectric constant owing to the conductivity relaxation with varying dispersant concentrations. The electromagnetic interference shielding effectiveness (EMI-SE) of the PANI/$ZnWO_4$ nanocomposites were found to be increased from -14 dB to -21 dB with enhancing wt% of $ZnWO_4$ in the PANI matrix. The composite samples displayed practically relevant shielding effectiveness in the entire microwave, X-band covering 8 to 12 GHz. The overall attenuation of the incident EM energy was around 99%, which is highly suitable for diverse EMI shielding applications. The nature of mild steel (MS) metal corrosion in 5 M HCl solution in the unprotected and protected system was studied by using SEM, AC impedance spectroscopy, potentiodynamic polarization (Tafel plots), and atomic absorption spectroscopy (AAS) techniques. The preliminary results indicate the mixed-type anticorrosion behavior. The AAS, AC impedance spectroscopy, and SEM results support the potentiodynamic polarization results.

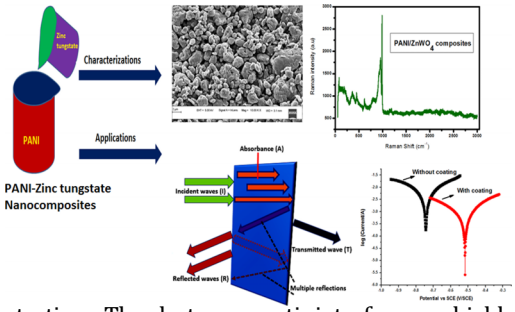

Keywords: nanocomposite, Raman spectroscopy, electric properties, EMI shielding, anticorrosion behavior.

1. Introduction

Controlling the wide spectrum of unwanted electromagnetic (EM) radiation and reducing EM emissions has become increasingly important due to the rapid growth of portable electronic devices, distributed electronic sensor arrays, and wireless communications. Shielding against electromagnetic interference is much needed to ensure that, electronics work safely without causing harm to people's health. Various frequency ranges and system types necessitate the different EMI shielding solutions.[1,2] Lightweight, high electromagnetic interference (EMI) shielding effectiveness (SE), simple processability, exceptional mechanical strength, and large absorption band are all desirable properties in EMI shielding materials. Intrinsic conducting polymers have the benefits of being simple to process, having high corrosion resistance, and being lightweight. They can be used in sensors, electrochromic materials, chemical power sources, and are particularly useful in the wide area of EMI shielding.[3]

Conducting polymers (CPs) such as polyaniline (PANI), polyacetylene, polypyrrole, polythiophenes polyparaphenylene, polyparaphenylene vinylene (PPV), and polyorthotoluidine have shown promising application potential in various domains of material science.[4,5] Among these, polyaniline[6-8] has sparked a lot of interest, because of its unique properties like easy synthesis, low price,

Acknowledgment: The authors are grateful to PES University, Bengaluru-560100, India, and the Oxford College of Engineering, Bommanahalli, Bengaluru-560068, India, for the support and encouragement. We would like to thank CeNSE, MNCF, IISc Bangalore for providing sample characterization facility.

***Corresponding Authors:** Muhammad Faisal (muhammadfaisal@pes.edu), Narasimha Raghavendra (rcbhat3@gmail.com), N. Maruthi (marutipnm@gmail.com)

environmental stability and tunable electrical conductivity. Chemical, magnetic, optical, and electrical properties of PANI can be modified and optimized for technological applications like LEDs, sensors,[9] antifouling, electromagnetic interference shielding, and anti-corrosion coatings.[4,10] As there is ever increasing demand for smart materials, optimizing the design of suitable conducting polymer-based composite structures is quite important for different applications. The CPs composites with appropriate dispersants can overcome the limitations with improved functionality originating due to the expected synergy of the composite phases.[11,12] Zinc tungstate has unique physico-chemical properties and is widely used in lithium-ion storage, X-/γ-ray scintillators, pseudo-capacitors, catalysis, and luminous devices, due to its energy transfer from $[WO_6]^{6-}$ to doped activator ion and effective absorption of ultraviolet (UV) excitation.[13-15] $ZnWO_4$ is an inorganic semiconductor, monoclinic tungstate with physical, chemical, optical, and mechanical properties that are relatively stable.[16] They are distinguished by a high refractive index, ecological friendliness, large X-ray absorption coefficient, a low price, and a low decay period. As a result, $ZnWO_4$ has been researched and optimized for a variety of utilization, including various sensor studies, AC and DC conductivity studies, photocatalysis, optical fibers, supercapacitor, and microwave applications.[17,18] The present work is aimed at the processing of PANI/$ZnWO_4$ nanocomposites for relevant multifunctional applications, mainly for broad band EMI shielding and corrosion inhibition.

Mild Steel (MS) metal is greatly employed in various industrial units because of its superior and unique mechanical properties compared to other metals. But, the utmost task with the use of MS metal is its proneness to disintegration.[19] Aggressive electrolyte solutions such as HCl, H_2SO_4, and $NO_3HNhHNO_3$ solutions are mainly used for various industrial operations such as cleaning, acid pickling, acid descaling, and oil-well acidizing. This causes corrosion of mild steel, which decreases the efficiency of the metal. Hence, the prevention of the dissolution of mild steel is very much essential.[20] Previously, species like nitrates, phosphates, nitrates, and chromates are widely used as anti-corrosion compounds for iron, aluminum, zinc, nickel, and copper in a corrosive electrolyte solution. But, these compounds are toxic to the environment and living creatures.[21,22] Hence, nowadays research has been shifted towards the development of eco-friendly anti-corrosion compounds. Literature study confirms that there are no reports on the suitability of ZnWO4 based conducting polymer composite as an anti-corrosion substance for MS metal in 5 M hydrochloric acid system with EMI shielding characteristics. PANI/ZnWO4 nanocomposites have been synthesized and studied the anticorrosion behavior on MS metal in 5 M hydrochloric acid atmosphere through SEM, AC impedance, electrochemical Tafel plots, and AAS techniques. Also, the EMI shielding performance contributed by the mechanisms of absorption and reflection is also analyzed.

2. Experimental

2.1. Materials used

In the present work, the materials used are aniline monomer (>99% pure), ammonium persulphate, ethanol, acetone, zinc tungstate, and hydrochloric acid (HCl). All these chemicals were procured from Sigma Aldrich (Merck), (Bengaluru, India). All the chemicals used in the present investigation are research grade. Double distilled water is employed for the synthesis process.

2.2. Synthesis and processing of PANI/$ZnWO_4$ nanocomposites

In-situ chemical oxidative polymerization technique was used to make PANI/$ZnWO_4$ nanocomposites, which is one of the most widely established synthesis method. 0.5 M aniline monomer in a watery solution of 0.5 M HCl with vigorous stirring produces aniline hydrochloride. The polymerization was started by adding 0.5 M ammonium persulfate $[(NH_4)_2S_2O_8]$ drop by drop, to the above mixture at a regulated temperature of 273 K-278 K with continuous stirring and the reaction was continued for another 4-6 hours.[23,24] Similarly, the composites were synthesized by introducing the necessary weight percentage (wt%) of $ZnWO_4$ to the polymerization solution. The chosen wt% of $ZnWO_4$ was 10, 20, 30, and 40 wt%. The nanocomposites are named PZ1 (PANI+10 wt% of $ZnWO_4$), PZ2 (PANI+20 wt% of $ZnWO_4$), PZ3 (PANI+30 wt% of $ZnWO_4$), and PZ4 (PANI+40 wt% of $ZnWO_4$). PANI/$ZnWO_4$ nanocomposites were purified and thoroughly washed with deionized water, and acetone.[25,26] The obtained precipitate was dried in an oven at 323-343 K and ground into fine powder.

2.3. Characterization techniques

The synthesized composite samples of PANI/$ZnWO_4$ nanocomposites have been characterized by X-ray diffraction in the range of 5°-90° by the Rigaku Smart Lab, using Cu-Kα radiation with a wavelength of 1.54 Å, and scan rate of approximately 1° per minute with a 40 kV generator voltage and a 40-mA current. The structure and chemical functional moieties in the materials were recognized by using FTIR spectrometer (Nicolet iS50, Mumbai, India). The spectra were obtained at ambient temperature in the wavenumber of 400-4000 cm^{-1}. Scanning electron microscopy (ULTRA55, GEMINI Technologies) was utilized to investigate the topography and surface of the newly synthesized samples of PANI/$ZnWO_4$ nanocomposites. The acceleration voltage was set to 20 kV. Using an energy dispersive spectrometer, the elemental distribution mapping of PANI/$ZnWO_4$ nanocomposites was determined. The micro-Raman spectra (Lab RAM HR) were obtained in the wavenumber of 3000 to 50 cm^{-1} with a laser beam of 5320 Å.[27-29]

2.4. AC conductivity measurements

Dielectric parameters and Alternating Current (AC) conductivity studies for the PANI/$ZnWO_4$ nanocomposites were performed by using an HP 4248 LCR meter between 100 Hz to 1 MHz at 30 ℃. The following equations are employed to calculate the dielectric parameters and AC conductivity of the PANI/$ZnWO_4$ nanocomposites.

$$\sigma_{ac} = \frac{d}{AZ} \quad (1)$$

$$\varepsilon' = \frac{C_s d}{A\varepsilon_0} \quad (2)$$

$$\tan\delta = \frac{\varepsilon''}{\varepsilon'} \quad (3)$$

Where, Z = AC impedance (in Ω), A = area of the pellet (in m^2), d = pellet thickness (in cm), tan δ = loss tangent, σ_{ac} = AC conductivity (in S/cm), C_s = series capacitance (in F), ε_0 = permittivity of free space (in F/cm), ε' = dielectric constant (real), and ε'' = dielectric constant (imaginary).

2.5. EMI shielding measurements

The EMI shielding measurements were performed by transmission line waveguide technique in a vector network analyzer (HP, model 8510C, 45 MHz-50 GHz, made: USA) The transmission line waveguide technique is one of the most acceptable and accurate methods in assessing the shielding efficiency of small quantities of materials over a broad frequency spectrum.[26] The nanocomposite powder has been compressed into rectangular pellets of standard X-band (8-12 GHz) waveguide dimension (X-band waveguide standard: WR 90 with inside dimensions 2.286 cm × 1.016 cm) of thickness 1.5 mm. This processed rectangular pellets of PANI/$ZnWO_4$ nanocomposites fit well inside the X-band rectangular wave guide sample holder of the Vector Network Analyzer.

2.6. Corrosion studies

AAS studies were carried out through exposure of precleaned Mild Steel (MS) in a beaker containing 100 ml of corrosive solution (5 M HCl) without and with a coating of PANI/$ZnWO_4$ nanocomposites at room temperature as per the ASTM procedure.[30] PANI/$ZnWO_4$ nanocomposites were applied to MS steel of 1 cm^2 area *via* drop-casting technique for coating. The PANI/$ZnWO_4$ nanocomposites were successfully cured on the MS surface by ultra-violet light shining for one hour at ambient temperature. After that, PANI/$ZnWO_4$ nanocomposites thickness layer was measured as 18 μm.[31,32] Coating effectively blocks the effective contact between MS and corrosive solution. Both potentiodynamic polarization (Tafel plots) and AC impedance spectroscopy (Nyquist plots) were performed with the help of CHI660C workstation by exposing 1 cm^2 of MS surface without and with coating in a 5 M HCl system. For this purpose, three electrodes are used (the working electrode is MS metal, the counter electrode is graphite electrode, and the reference electrode is saturated calomel electrode). Prior to the potentiodynamic polarization (Tafel plots) and AC impedance spectroscopy (Nyquist plots) test, the MS was exposed to a 5 M hydrochloric acid system for approximately 1 h to achieve the steady-state Open Circuit Potential (OCP). Tafel curves were recorded in the potential range of (±250 mV) with a scan rate of 0.1 mV/s.[26] Whereas Nyquist plots were obtained in the frequency of 10^5-10^{-2} Hz. Surface topography of MS without and with coating system was studied by using the SEM technique. The protection efficiency (observed from AAS, potentiodynamic polarization (Tafel plots), and AC impedance spectroscopy (Nyquist plots)) was calculated as per the procedure stated in the literature.[20,33]

3. Results and discussion

3.1. FTIR spectra

Figure 1 depicts the FTIR spectra of PANI, $ZnWO_4$, and PANI/$ZnWO_4$ (10, 20, 30, and 40 wt%) nanocomposites. The leading bands in refined PANI are typical polyaniline bands (observed at 1568, and 1472 cm^{-1}). These are allotted to the stretching of C=C deformation of the benzenoid ring. FTIR bands at 1279 and 1245 cm^{-1} are assigned to stretching of C=N deformation of benzenoid ring. Bands around 1121 and 1040 cm^{-1} are attributed to C-H in-plane bending vibration. Further, the presence of C-H out of plane bending flexural vibrations in the benzene ring of PANI was confirmed by the existence of a band at 799 cm^{-1}.[34,35] The FTIR spectrum of pristine $ZnWO_4$ is displayed in Figure 1. The main bands are as follows; 3417, 1615, 1164, 1093, 814, 709, 606, 572, 453, and 426 cm^{-1}. The bands at 3417 and 1615 cm^{-1} correlated to the existence of H_2O molecules absorbed on the $ZnWO_4$. The major absorption bands for $ZnWO_4$ are observed at 426 and 1156 cm^{-1}. The bands at 814 and 709 cm^{-1} are caused by stretching modes of W-O in the WO_6 octahedron, while the band at 606 cm^{-1} is caused by the symmetrical motions of the bridged oxygen atoms in the Zn-O-W group. The band pinpointed at 556 and 453 cm^{-1} are due to the longer W-O bond (in-plane deformation modes).[36,37] The FTIR spectrum of PANI/$ZnWO_4$ nanocomposite (PZ1) shows bands at 2330, 2116, 1917, 1558, 1468 and 1290 cm^{-1}. The spectrum of PZ2 is at 2327, 2113, 1929, 1554, 1468, and 1290 cm^{-1}. The bands of PZ3 are at 2338, 2112, 1925, 1558, 1469, and 1295 cm^{-1}. The bands of PZ4 are at 2342, 2104, 1933, 1554, 1469, and 1295 cm^{-1}. The presence of bands of both PANI and $ZnWO_4$ in the nanocomposites reveals the conjugated structure of polyaniline chains and their associa-

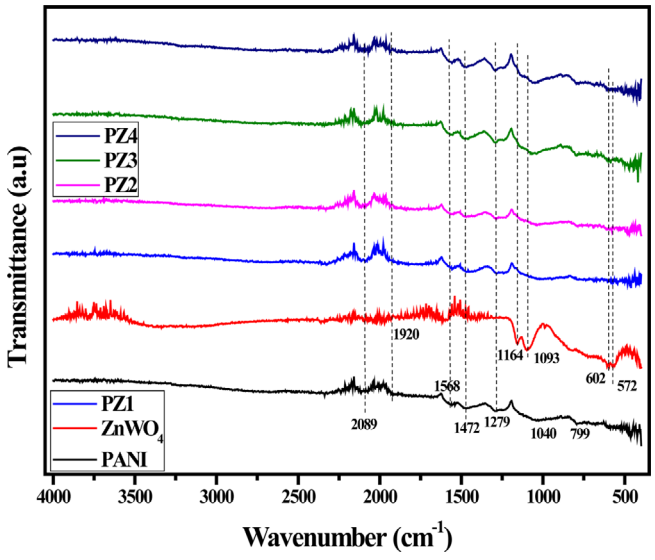

Figure 1. FTIR spectra of PANI, $ZnWO_4$, and PANI/$ZnWO_4$ nanocomposites.

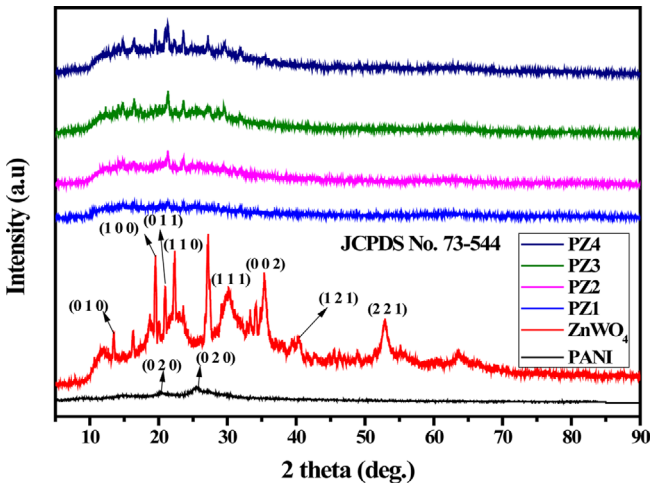

Figure 2. XRD pattern of PANI, $ZnWO_4$, and PANI/$ZnWO_4$ nanocomposites.

tion with $ZnWO_4$. Thus, the emergence of the PANI/$ZnWO_4$ composite is observed. The shift in characteristic polyaniline peaks indicates the incorporation of $ZnWO_4$ in polyaniline matrix. The characteristics peaks of $ZnWO_4$ were not observed due to lower content wt% of $ZnWO_4$ in PANI, however two pair of broad peaks at 1164 and 1093 cm^{-1} for higher wt% of $ZnWO_4$ in PANI (PZ3 and PZ4) were clearly observed. Similar trend was observed in the literature.[38] The $ZnWO_4$ content in PANI was also confirmed by XRD studies (Figure 2).

3.2. X-ray diffraction studies

Figure 2 shows XRD patterns of PANI, $ZnWO_4$, and PANI/$ZnWO_4$ nanocomposites with chosen concentration (in wt%) of $ZnWO_4$. The XRD pattern of PANI shows the typical semi-amorphous nature, with broad peaks appearing at 2θ=20° and 25.48° are corresponding to the planes (0 2 0), and (2 0 0).[35] ZnWO4 has shown the characteristic crystalline peaks and PANI/ZnWO4 nanocomposites have shown modified structural features confirming the composite formation. The characteristic diffraction peaks of the pure $ZnWO_4$ at 2θ = 13.50°, 19.54°, 20.95°, 22.5°, 30.13°, 35.35°, 38.13°, 40.57°, and 52.96° are due to (010), (100), (011), (110), (111), (002), (200), (121), and (221) planes of $ZnWO_4$ respectively. According to JCPDS No. 73-544, fabricated sample is single-phase.[39] PZ1 shows diffraction peaks (10%) at 2θ = 13.43°, 21.58°, 27.03°, and 29.75°. Whereas, PZ2 (20%) shows peaks at 2θ = 13.86°, 21.58°, 27.24°, and 29.96°. The diffraction peaks at 2θ = 13.86°, 21.38°, 27.44°, and 29.89° are assigned to PZ3 (30%). Further, PZ4 (40%) explores diffraction peaks at 2θ = 13.64°, 21.38°, 27.24°, and 30.06°. This indicated that the structure of $ZnWO_4$ has been preserved with an enhancement in the amount of $ZnWO_4$. The position of characteristic peaks in $ZnWO_4$ and PANI/$ZnWO_4$ nanocomposites are unchanged with modified intensity.[40]

The equation gives Bragg's condition for diffraction

$$n\lambda = 2d \sin\theta \quad (4)$$

Table 1. Grain size dimension of PANI, $ZnWO_4$, and PANI/$ZnWO_4$ composites

Sample	2θ (deg.)	FWHM (radians)	D (nm)	d (Å)	Q (Å)	R (Å)
PANI	20.46	0.01762992	7.991745	0.43373	1.448649	5.421592
	25.18	0.084061165	1.69008	0.35339	1.777962	4.417407
$ZnWO_4$	13.4672	0.009991137	13.97409	0.65695	0.956411	8.211933
	19.5415	0.005885599	23.90493	0.4539	1.384262	5.673769
	20.9731	0.007476467	18.8604	0.42323	1.484577	5.290385
	27.211	0.01105317	12.90645	0.32746	1.918769	4.09324
	30.1766	0.066742438	2.151624	0.29592	2.123276	3.698993
	35.3509	0.023616399	6.161987	0.2537	2.476608	3.171266
	40.3821	0.048010517	3.077089	0.22318	2.815334	2.789716
	52.9192	0.030347611	5.103454	0.17288	3.6344	2.161012
PZ1	14.1217	0.016052142	8.703733	0.62665	1.002662	7.833131
	21.239	0.039235874	3.595438	0.41799	1.503184	5.224899
	28.704	0.008884249	16.10948	0.31076	2.021895	3.884466
	29.4198	0.012745441	11.24736	0.30336	2.071217	3.791965
PZ2	14.224	0.022488567	6.213338	0.62217	1.009888	7.777081
	21.3413	0.021388835	6.596611	0.41601	1.51034	5.200141
	25.6158	0.109807564	1.294919	0.34748	1.808224	4.343478
PZ3	14.8171	0.032805907	4.262075	0.59739	1.051767	7.467413
	21.3617	0.014574896	9.680931	0.41562	1.511767	5.195233
	27.1088	0.083527967	1.707529	0.32867	1.911698	4.108381
	29.4607	0.018195057	7.879392	0.30295	2.074033	3.786817
PZ4	14.2035	0.054078154	2.583778	0.62306	1.00844	7.788248
	21.3413	0.016939468	8.329295	0.41601	1.51034	5.200141
	27.1701	0.064600744	2.2081	0.32794	1.915939	4.099286
	29.6244	0.057470202	2.495554	0.30131	2.0853	3.766356

$$d = \frac{n\lambda}{2\sin\theta} \quad (5)$$

$$D = \frac{k\lambda}{\beta\cos\theta} \quad (6)$$

$$R = \frac{5\lambda}{8\sin\theta} \quad (7)$$

$$Q = \frac{4\pi\sin\theta}{\lambda} \quad (8)$$

Where λ is the X-ray wavelength, θ is the glancing angle, d is the interplanar spacing, and n is the spectrum order. β is full-width half maxima and D is the grain size. The interplanar distance (d) is calculated by using Bragg's law and the average intercrystalline separation (R), and Structure factor (Q) for the synthesized samples have been calculated using the respective equations.[41] As per the grain size dimension data calculated in Table 1, it is confirmed that the particles are in nano size. From Table 1, the polyaniline synthesized in the present work has an average grain size of 4.84 nm, zinc tungstate has an average grain size of 10.766 nm. The nanocomposites have average shown grain sizes of 9.91475 nm, 4.7016 nm, 5.8825 nm, and 3.9042 nm respectively for PZ1, PZ2, PZ3, and PZ4 samples.

3.3. Raman spectroscopy analyses

Raman spectroscopy is an effective technique for investigating the vibrational modes of lattices and molecules. The structure of PANI/$ZnWO_4$ nanocomposites was further investigated using the Raman spectra. According to several studies, the vibrational modes of $ZnWO_4$ contain 36 patterns.[42] As shown in Figure 3, Raman analysis was performed on the highly crystalline samples. Curve PZ1, PZ2, and PZ3 denote the spectra for PANI/$ZnWO_4$ (10, 20, and 30 wt%) nanocomposites, respectively. The spectra revealed very high intensity and sharp peaks, but identical spectral characteristics. Bands of Raman spectroscopy can be observed at 191, 356, 400, 454, 613, 807, and 952 cm^{-1}. The most powerful band was found at 952 cm^{-1}, and it was caused by internal stretching modes is due to the W-O bond in the WO_6 octahedra. Six internal stretching modes are attributed to the 191, 356, 400, 454, 613, and 807 cm^{-1} bands.[23,36,43] The

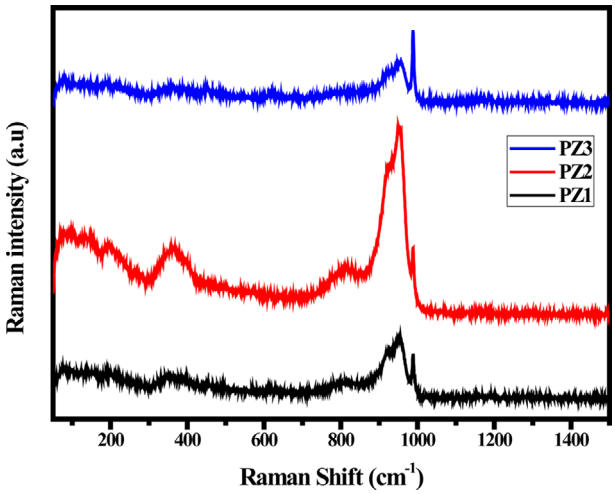

Figure 3. Raman spectra of PANI/$ZnWO_4$ nanocomposites.

spectra of the composites exhibit the identical intensity variations of PANI/$ZnWO_4$. This validates the dispersant $ZnWO_4$ presence in the polyaniline matrix.

3.4. Scanning electron micrograph

Figure 4(a)-(f) shows the SEM microstructure of pure PANI, $ZnWO_4$, and PANI/$ZnWO_4$ nanocomposites (10, 20, 30, and 40 wt.%) respectively. The micrograph revealed the variation in surface morphology and distribution of $ZnWO_4$ in PANI nanocomposites. The immaculate PANI has a granular aggregation and dissimilar shape (Figure 4(a)). The most common morphology for PANI produced in acidic aqueous media is spherical morphology.[25,44] Figure 4(b) demonstrates that the prepared sample has a distinct shape and ZnWO4 was dispersed evenly across the porous structure. The $ZnWO_4$ particles joined and produced a larger plate sheet.[45] Figure 4(c)-(f) reveals the presence of $ZnWO_4$ in a PANI/$ZnWO_4$ nanocomposite, and it has a homogeneous distribution with varying grain sizes. The nanocomposites have a porous and granule structures. Furthermore, due to the varying grain size of $ZnWO_4$, the composites have effective interfaces that are related to one another.[46-48] As a result, the nanocomposites are expected to facilitate the electromagnetic shielding efficiency by intense interaction with the incident electromagnetic energy and anticorrosion properties.

3.5. TEM studies

Figure 5 shows the transmission electron microscope images of PANI, PANI/$ZnWO_4$ (30%) nanocomposites. The dimensional range of the nanocomposites are in nano scale,[49] which was confirmed by XRD data analysis (Table 1). It is evident that the addition of $ZnWO_4$ in polyaniline increases the size of PANI/$ZnWO_4$ particles. Figure 5(a) shows a microporous spherical structure with polymer chain.[50] The microporous spherical structure of the PANI nanocomposites (Figure 5(a)) has a diameter of about 10 nm. When self-made $ZnWO_4$ nanoparticles are combined with PANI, the microporous PANI is most likely polymerized on the surface of the $ZnWO_4$ particles. Thus, $ZnWO_4$ particles having a diameter of around 15 nm were incorporated into the polyaniline matrix as evidenced in (Figure 5(b)) for the TEM image PANI/$ZnWO_4$ nanocomposite.

3.6. AC conductivity and dielectric properties

The low frequency AC electrical conductivity of PANI, $ZnWO_4$, and PANI with incorporated $ZnWO_4$ in different wt% is illustrated in Figure 6. It is clear from the graph that, all the samples exhibited strong frequency dependence at a high-frequency region above critical frequency (10 kHz) due to its dielectric nature. The observed trend is on par with recent literature owing to the effect of both the intrinsic dipole polarization and the Maxwell-Wagner-Sillar effect. The rise in conductivity is because the charge carriers get appropriate energy to overcome the potential barrier created due to the combined PANI and $ZnWO_4$ segments. Whereas, the conductivity is constant below critical frequency for which charge carriers don't get enough energy to

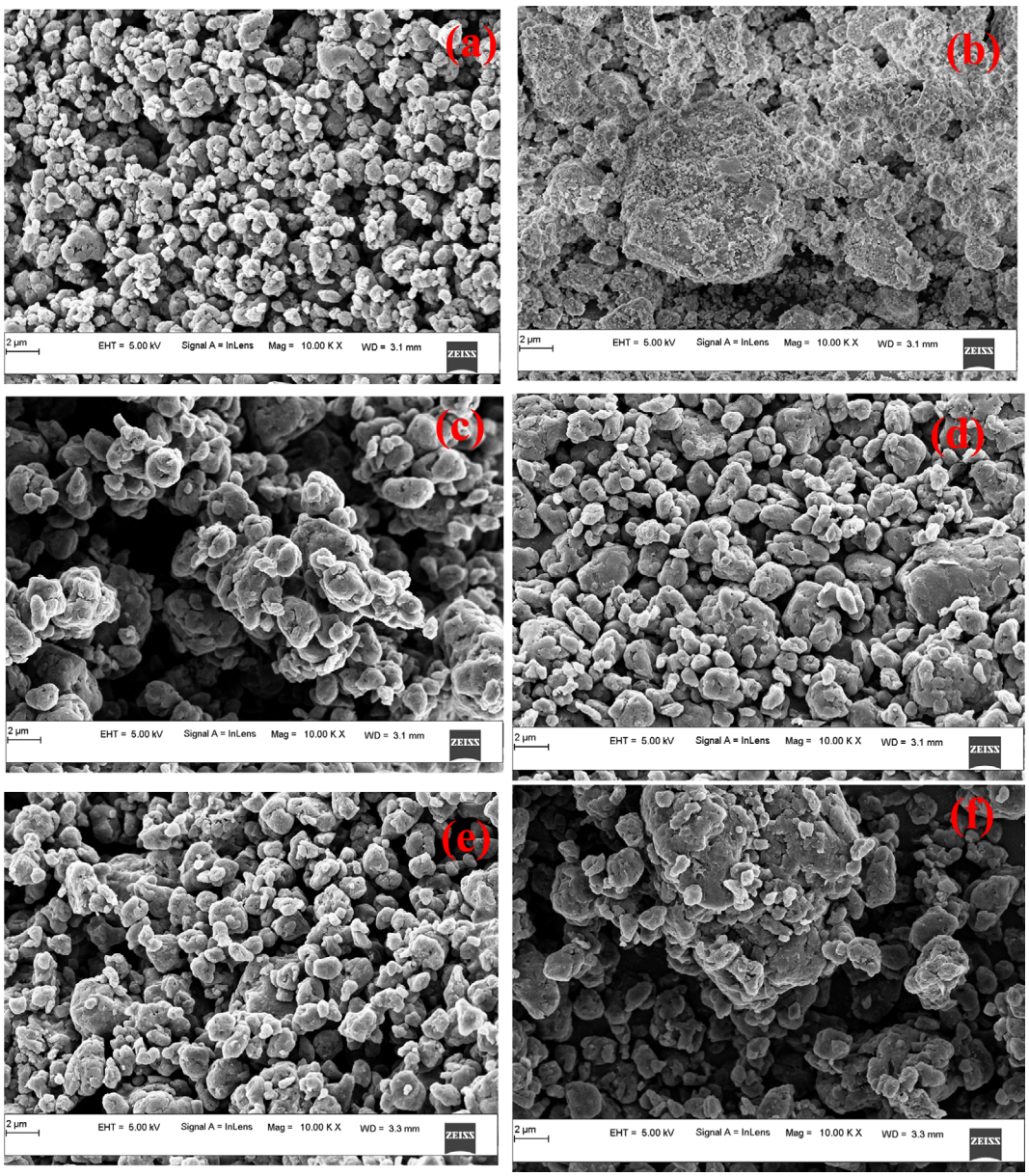

Figure 4. SEM topography of (a) PANI, (b) $ZnWO_4$, (c-f) PANI/$ZnWO_4$ nanocomposites.

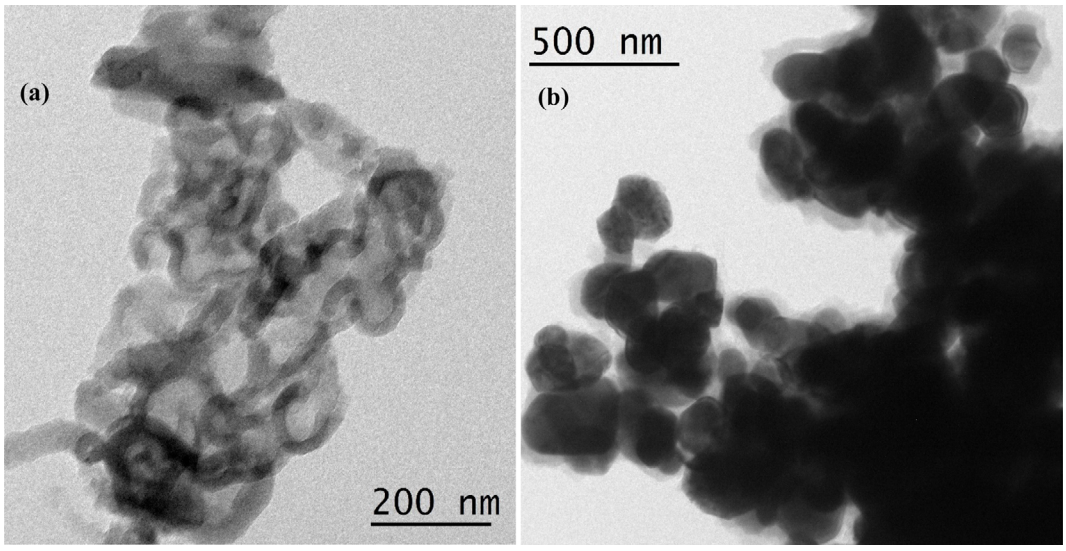

Figure 5. TEM images of (a) PANI and (b) PANI/$ZnWO_4$ nanocomposite (PZ3-30%).

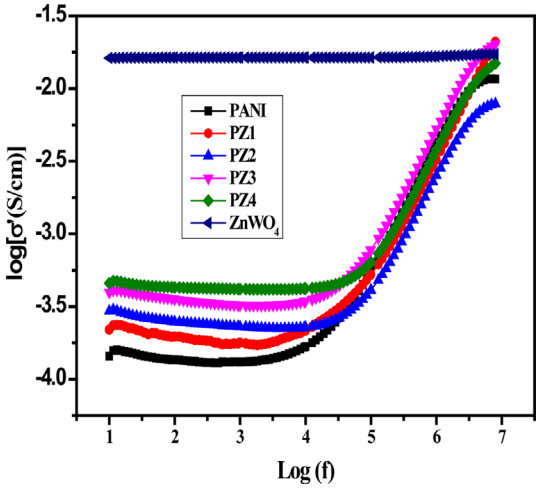

Figure 6. The response of the real part of AC conductivity versus various applied frequencies for PANI, $ZnWO_4$, and PANI/$ZnWO_4$ composites.

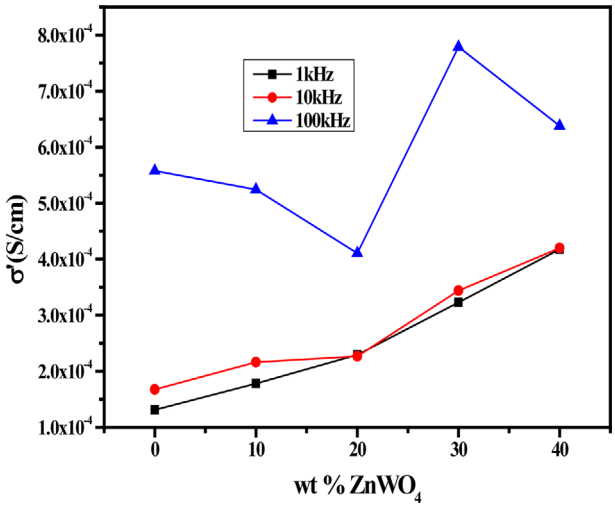

Figure 7. Variation of AC conductivity of PANI/$ZnWO_4$ composites with varying concentration (wt%) of $ZnWO_4$ at selected frequencies (1, 10, and 100 kHz).

knock out the potential barrier.[51] Figure 7 explores the dependency of AC conductivity on PANI with (10, 20, 30, and 40 wt%) of $ZnWO_4$ in PANI at constant frequencies (1, 10, and 100 kHz). It is evident from the analysis that, not much variation in conductivity is observed in the range of frequency of 1 kHz and 10 kHz. This is the region of frequency-independent conductivity as shown in Figure 6. Further, for 100 kHz frequency, the conductivity is decreased for the samples up to 20 content wt% of $ZnWO_4$ in PANI, and conductivity is enhanced for 30 wt% and again it's decreased for 40 wt% of $ZnWO_4$ in PANI. This tunability in the observed electrical conductivity is an indication of the dependency of electrical properties on percolation threshold. At 30 wt% composition, PANI/$ZnWO_4$ composite structure has shown by intense bridging in the conducting network. The conductivity of these polymer composites is tunable with varying concentration of the dispersant and the resulting changes in the surface morphology of the polymer matrix can facilitate various property responses. At 40 wt% loading of $ZnWO_4$ in PANI, the composite shows higher crystalline region in the sample, which prevents ion migration and as a result a slight decrease in conductivity. Also, the combination of PANI with $ZnWO_4$ forms strong aggregates at 40 wt% loading of $ZnWO_4$ causing additional reduction of conductivity.

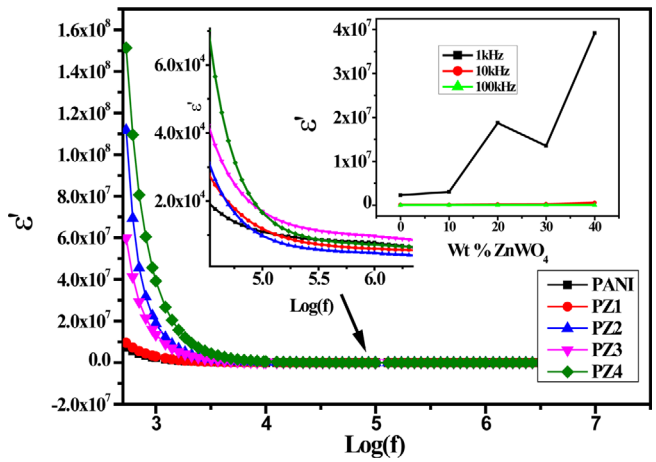

Figure 8. The dielectric constant v/s frequency of PANI and PANI/$ZnWO_4$ nanocomposites.

Inset 1: Magnified view of dielectric constant response of samples at high frequencies. *Inset 2:* The dependency of dielectric constant of PANI/$ZnWO_4$ composites at selected frequencies (1, 10, and 100 kHz)

The dielectric constant of PANI and PANI/$ZnWO_4$ nanocomposites samples is shown in Figure 8. As seen from the graph, the obtained large dielectric constant at lower frequency is attributed by either the Maxwell-Wagner effect or increasing mobility of charge carriers, or both. The dielectric constant of dielectric materials can be described by the dielectric relaxation mechanism. At lower frequencies, all ionic, atomic, or electronic, orientation, and interfacial mechanisms contribute to the polarization effect and hence materials exhibit large dielectric constant values. At higher frequencies, only the electronic polarization mechanism contributes to the total polarization and other mechanisms seize out due to high frequency and hence small dielectric constant. *Inset 1* of Figure 8 shows the dispersed change in dielectric constant at higher frequencies. *Inset 2* of Figure 8 confirms the dependency of dielectric constant on PANI with four different wt% of $ZnWO_4$ at selected frequencies. The dielectric attributes of the composites samples are found to be $ZnWO_4$ concentration dependent and large dielectric constant is observed in the case of 40 wt% of $ZnWO_4$ in the PANI nanocomposites sample due to the developed dipole action with increase in the segment mobility of the nanocomposite.

Another relevant electrical parameter tangent loss (tan δ) is defined in terms of real (ε') and imaginary (ε'') parts of the dielectric constant. The tan $\delta = \varepsilon''/\varepsilon'$ verses applied frequencies observed for these composites are shown in Figure 9. The values of tangent loss are higher at lower frequencies, and is declined with increasing frequency. The tangent loss values are almost constant at higher frequencies, which is similar to the dielectric constant response. The reduced loss tangent at observed at higher frequencies is attributed to the weak space charge polar-

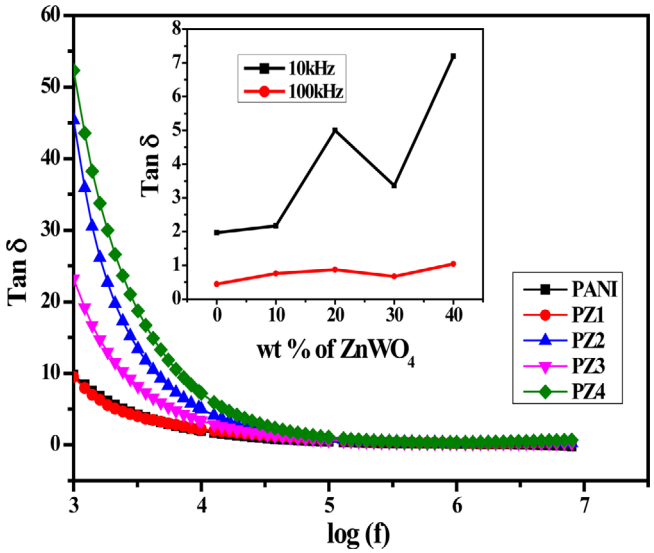

Figure 9. The tangent loss (tan δ) response v/s AC frequency for PANI and PANI with four different wt% of $ZnWO_4$. *Inset:* The dependency of tangent loss (tan δ) on four different wt% $ZnWO_4$ in PANI at constant frequencies (1, 10, and 100 kHz).

ization for a large number of dipoles at the interfaces between the two segments. These dipoles cannot orient in the direction of the electric field. *Inset* of Figure 9 reveals the dependency of tan δ on four different wt% of $ZnWO_4$ in PANI at selected frequencies. The observed high tangent loss at 40 wt% of $ZnWO_4$ in the PANI matrix owing to the enhance in the number of self-associated bonds generated by the intermolecular interaction during the formation of nanocomposites. The formed discrete aggregates are minimal at the threshold content (20 and 30 wt%) of $ZnWO_4$ in PANI lowering the tan δ which is also supported by AC conductivity studies (Figure 7).

The Cole-Cole plots for all the prepared PANI/$ZnWO_4$ nanocomposite samples are displayed in Figure 10. This figure shows that, PANI and PANI/$ZnWO_4$ nanocomposites shows closely

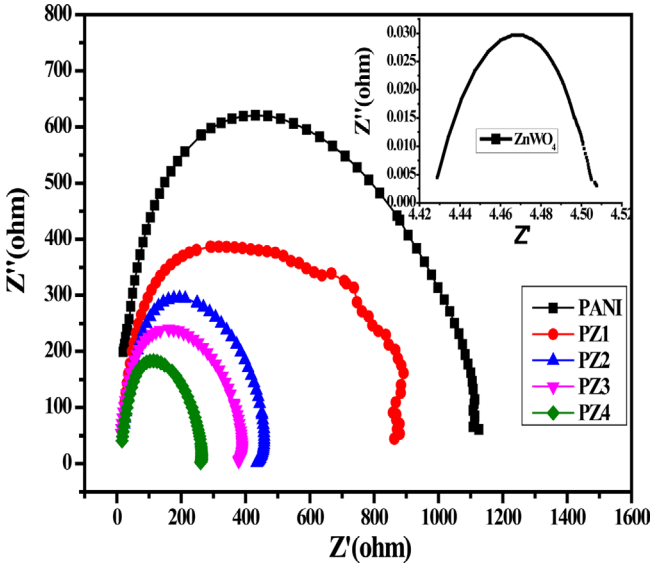

Figure 10. Complex impedance of PANI and PANI/$ZnWO_4$ nanocomposites.

semicircles with slight variations. This is representative of a superlative dielectric system. The area under the semicircle provides bulk resistivity to the system.[52] It has been observed from the figure that, pure PANI provides high ionic bulk resistivity and pure $ZnWO_4$ gives negligible ionic bulk resistivity (*inset* of Figure 10) due to high conductivity species. In addition, the semicircle shape of the plot is the proof of related relaxation following the Debye model of single relaxation. The decrease of radius of the semicircles by with varying loading of $ZnWO_4$ in PANI indicates the decreasing of bulk ionic resistivity and increasing conductivity of the samples.

3.7. Microwave shielding properties

The diverse and intense array of unwanted electromagnetic waves from various electro/electrical systems and wireless devices interacts with the shielding material to ensure the required suppression and attenuation of the electromagnetic pollution. This induced electromagnetic field modifies the total field and changes the direction of charge motion. Generally, when EM energy incident on the shielding material, a portion of the wave is reflected due to the interaction of surface charges. As this interaction and the subsequent attenuation of the EM energy is facilitated by the mobile charge carriers, the material utilized as an EMI shielding material should be conducting in nature.[53] The recorded values of scattering parameters are used to calculate the specific absorption and reflection contributions of the samples and also to calculate the total shielding efficiency.[54] The schematic representation of the EMI shielding mechanism is shown in Figure 11.

The reflection (R), transmission (T), and absorption (A) coefficients are determined by using the Eqs. (9)-(11).[55,56]

$$R = |S_{11}^2| = |S_{22}^2| \tag{9}$$

$$T = |S_{12}^2| = |S_{21}^2| \tag{10}$$

$$A = 1 - R - T \tag{11}$$

Where S_{11}, S_{22}, S_{12}, and S_{21} are scattering parameters. The shielding effectiveness due to reflection (SE_R), and absorption (SE_A) are calculated using Eqs. (12)-(13).

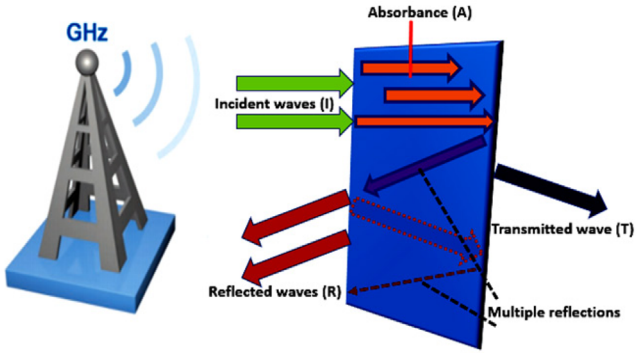

Figure 11. Schematic representation of EMI shielding mechanism with its components.

$$SE_R = -\log_{10}(1-R) \quad (12)$$

$$SE_A = -\log_{10}\left\{\frac{T}{1-R}\right\} \quad (13)$$

The total shielding effectiveness is calculated using the below equations:

$$SE(dB) = -10\ \log\frac{P_t}{P_i} \quad (14)$$

$$SE(dB) = SE_R + SE_A + SE_M \quad (15)$$

Where, P_i and, P_t are the incident and transmitted electromagnetic powers, while SE_R, SE_A, and SE_M are shielding efficiency due to the reflection, absorption, and multiple reflections, respectively.

The EMI shielding efficiency of the synthesized PANI and PANI/$ZnWO_4$ nanocomposites were tested in the 8-12 GHz (X-band) frequency range and the observed shielding efficiency is shown in Figure 12. An EMI shielding material is conceptually a barrier to the transmission of electromagnetic energy and the efficiency of attenuation capabilities have been analyzed in terms of shielding efficiency (expressed in dB). Regulating the shielding mechanism by a material sample involves the complex interplay of various structural and morphological characteristics of the materials with tunable electrical characteristics. The attenuation capability of the composite samples is observed to be stable in the entire X-band frequency range and the results confirms that moderate concentration of the dispersant $ZnWO_4$ (10 to 30 wt%) in PANI matrix can be optimized with relevant shielding efficiency for practical electromagnetic compatibility applications. The obtained shielding results show that PANI/$ZnWO_4$ nanocomposites exhibit SE in the range of -19 to -21 dB for various concentration of $ZnWO_4$ in polyaniline. The maximum SE observed was ~ -21 dB for the PZ2-PZ4 composites and this corresponds to an overall electromagnetic energy attenuation of 99% by the PANI/$ZnWO_4$ nanocomposites. EMI shielding efficiency > -20 dB is the acceptable value of relevance as per the documented literatures on shielding indicating the suitability of a shield for broad band EMI shieling applications.[43] EMI shielding performance by materials have been found to be diverse in terms of the internal mechanisms by which the unwanted electromagnetic energy is shielded. To further understand the specific mechanisms of attenuation of EM energy by these composite samples, Figure 13 depicts the absorption (A) and reflection (R) contributions by the composite samples with specific interaction of the incident electromagnetic energy in the broad microwave range. According to the results, around 64-78% of EM energy has been absorbed indicating the dominant absorption nature with minimal reflection (22-36%). The shielding analysis clarifies that these composites can be optimized for broad band EMI shielding applications with microwave absorbing requirements.

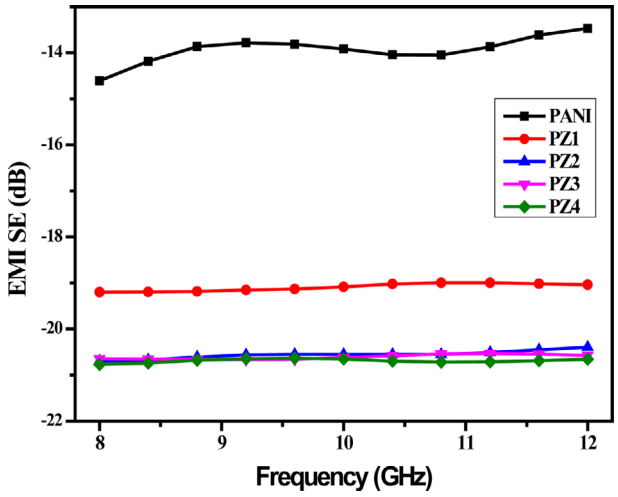

Figure 12. EMI shielding effectiveness of PANI and PANI/$ZnWO_4$ nanocomposites in the X-band (8-12 GHz) frequency range.

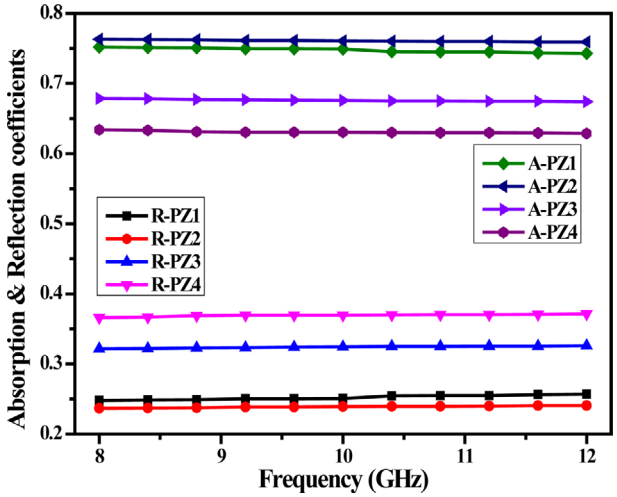

Figure 13. Absorption (A) and reflection (R) coefficient of PANI/$ZnWO_4$ nanocomposites in the X-band frequency range

3.8. Corrosion studies

AC impedance spectroscopy is the most effective technique for investigating the anticorrosive nature of polymer nanocomposites in an unprotected and protected system. Figure 14 and Table 2 show the Nyquist curves for MS metal in 5 M hydrochloric acid (corrosive solution) without and with a coating of various concentrations of polymer (PANI/$ZnWO_4$) nanocomposites. Careful analysis of Figure 14 and Table 2 shows the diameter of depressed semicircle enhanced with a coating of polymer nanocomposite and protection efficiency was enhanced with a rise in the zinc tungstate amount in polymer nanocomposite. Comparable observations were reported by Maruthi *et al.*,[57] The polymer coating on mild steel (MS) effectively isolates the metal surface from the corrosive electrolyte solution. This can be observed by the high charge transfer resistance value (R_{ct}) in the existence of polymer coating. The low R_{ct} without polymer coating clearly shows the aggressive nature of the 5 M HCl system on Mild Steel (MS) surface.

Electrochemical potentiodynamic polarization results are depicted in Table 3 and Figure 15. The results show that the mild steel (MS) corrosion current density values (i_{corr}) are less in the inhibited system (with coating) compared to an uninhib-

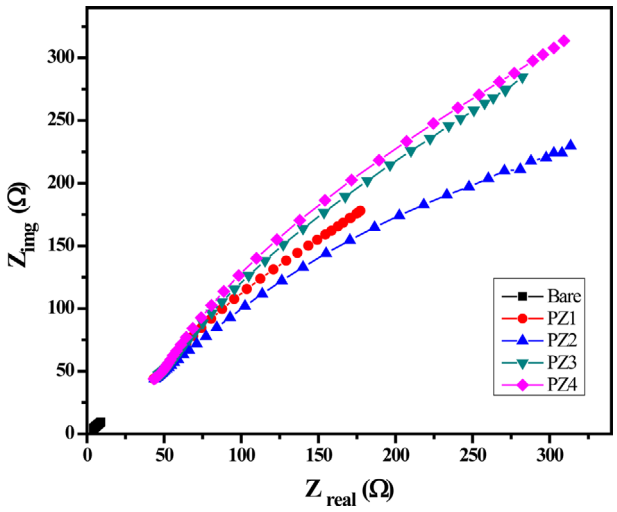

Figure 14. Nyquist plots without and with coating.

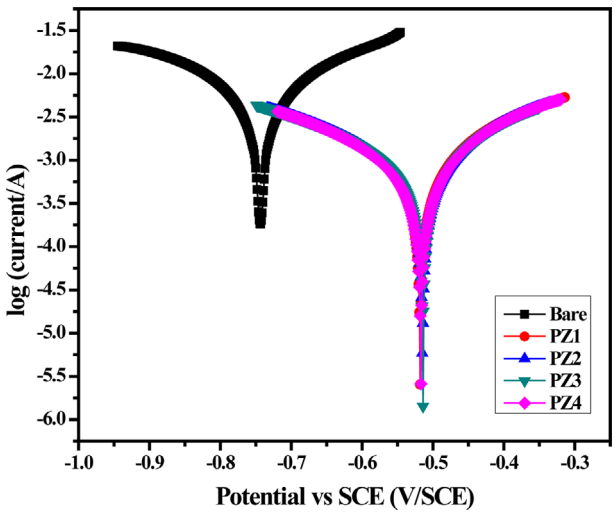

Figure 15. Tafel plots without and with a coating of polymer nanocomposite.

ited system (without coating). This is because, in the protected system (MS surface with polymer coating), as there is no direct contact between MS metal and 5 M HCl solution due to the presence of polymer nanocomposite on the metal surface. This polymer nanocomposite blocks the harsh nature of 5 M HCl on the metal surface. As a result of this, MS is inactive towards electrolyte solution. Hence, low corrosion current value is observed. This confirms the anticorrosive property of polyaniline nanocomposite on the MS surface. Further, in the present investigation, the variation in the mild steel corrosion potential (E_{corr}) value is lower than the 85 mV. Hence, Polymer (PANI/$ZnWO_4$) nanocomposite is represented as a mixed anticorrosion behavior on MS in studied corrosive solution.

The AAS results show that (Table 4), the presence of a nanocomposite coating on MS metal surface in 5 M HCl system decreases the iron content in corrosive solution. This is because; the presence of polymer coating on mild steel will act as a barrier for the dissolution process. Hence, the amount of iron content in corrosive solution is low in the protected system (with coating) when compared with an unprotected system (without coating). Similar observations were reported in the literature.[26] SEM results are shown in Figure 16. Without coating the conducting polyaniline composites, the MS surface becomes very rough with pits, due to the harsh nature of 5 M HCl on the metal surface. This allows direct interactions between MS and the 5 M HCl system. As a result of this, the weight loss of MS increases. Smooth MS surface is noticed in the presence of the nanocomposite coating on MS. This trend is because of the presence of the thick film on the MS metal surface in a 5 M HCl

Table 4. Results of AAS without and with coating

System	Iron amount dissolved in acid solution in mg/L	% Protection efficiency
Bare	87	
PZ1	41	52.874
PZ2	30	65.517
PZ3	19	78.161
PZ4	06	93.103

Table 2. Impedance spectroscopy results

System	Charge transfer resistance (Ω)	n	χ^2	PE (%)
Bare	13	0.850	6.701×10^{-4}	
PZ1	180.4	0.858	4.673×10^{-5}	92.793
PZ2	231.3	0.87	5.190×10^{-5}	94.379
PZ3	268.7	0.98	2.60×10^{-5}	94.940
PZ3	330.9	0.88	2.567×10^{-5}	96.071

Table 3. Tafel curve results

System	Corrosion potential (mV)	Cathodic Tafel slope (V/dec)	Anodic Tafel slope (V/dec)	Corrosion current (A) $\times 10^{-3}$	PE (%)
Bare	-733	4.513	4.971	6.415	
PZ1	-518	4.779	5.563	0.832	87.030
PZ2	-515	4.738	5.631	0.814	87.310
PZ3	-513	4.760	5.640	0.798	87.756
PZ4	-517	5.013	5.730	0.737	88.511

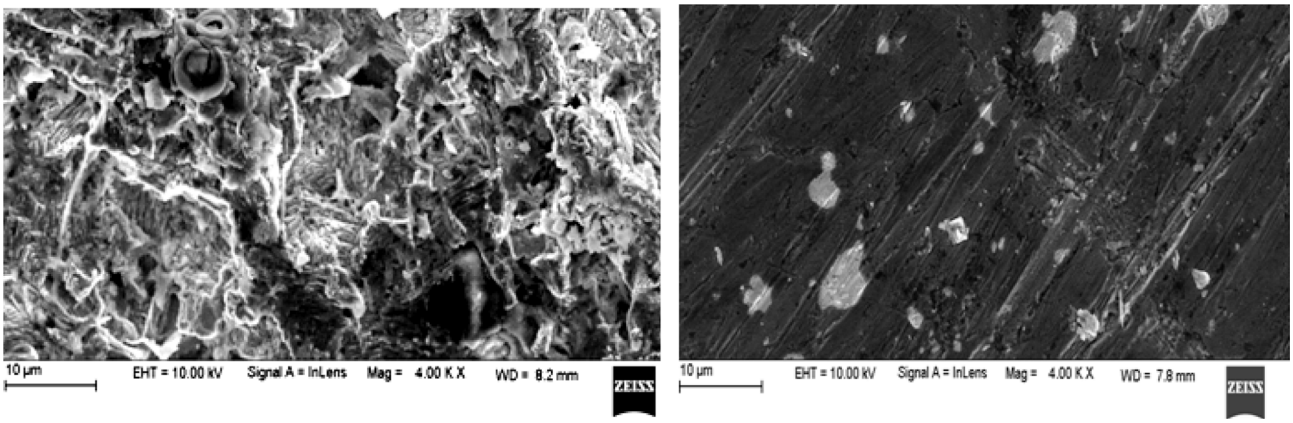

Figure 16. SEM images of unprotected and protected system.

atmosphere. This avoids the direct interaction between 5 M HCl solution and MS surface.

4. Conclusions

The *in-situ* polymerization method is successfully used to fabricate the PANI/$ZnWO_4$ samples, and structural characteristics were studied by using FT-IR, XRD, Raman spectra, and electron microscopy (SEM and TEM). Creation of the efficient composite network with synergistic interactions allowing charge transfer between PANI and $ZnWO_4$, the composites have shown modified electrical conductivity and dielectric attributes. The EMI shielding capabilities of these composites in the broad microwave X-band (8-12 GHz) range of practical significance were found to be in the acceptable range of -19 to -21 dB, signifying 99% attenuation. The higher weight percentage composite samples have shown similar efficiency indicating that these composite materials exhibit relevant shielding efficiency with moderate concentrations in weight percentage of the dispersant $ZnWO_4$. Also, it is observed that the mechanisms of attenuation the electromagnetic energy by reflection and absorption is different at different loading of $ZnWO_4$. Tafel plots results showed a mixed anticorrosive nature of polymer nanocomposite on MS metal in 5 M HCl atmosphere. The iron content found to be low in 5 M HCl environment with the coating of polymer (PANI/$ZnWO_4$) nanocomposite. SEM results reconfirms the Tafel plots, Nyquist plots, and AAS results. The observed shielding efficiency with the anticorrosive response of electrically modified PANI/$ZnWO_4$ nanocomposite samples can be further optimized as promising multifunctional EMI shields.

Conflict of interest: The authors declare no conflict of interest.

References

(1) Z. Barani, F. Kargar, K. Godziszewski, A. Rehman, Y. Yashchyshyn, S. Rumyantsev, G. Cywiński, W. Knap, and A. A. Balandin, *ACS Appl. Mater. Interfaces*, **12**, 28635 (2020).
(2) D. Jiang, V. Murugadoss, Y. Wang, J. Lin, T. Ding, Z. Wang, Q. Shao, C. Wang, H. Liu, N. Lu, R. Wei, A. Subramania, and Z. Guo, *Polym. Rev.*, **59**, 280 (2019).
(3) Y. Zhang, L. Wang, J. Zhang, P. Song, Z. Xiao, C. Liang, H. Qiu, J. Kong, and J. Gu, *Compos. Sci. Technol.*, **183**, 107833 (2019).
(4) T. Machappa and M. V. N. Ambika Prasad, *Ferroelectrics*, **392**, 71 (2009).
(5) S. Iqbal and S. Ahmad, *J. Ind. Eng. Chem.*, **60**, 53 (2018).
(6) K. Yamabe and H. Goto, *Macromol. Res.*, **26**, 704 (2018).
(7) S. Benhouhou, A. Mekki, M. Ayat, and N. Gabouze, *Macromol. Res.*, **29**, 267 (2021).
(8) S. L. Madaswamy, S. M. Wabaidur, M. R. Khan, S. C. Lee, and R. Dhanusuraman, *Macromol. Res.*, **29**, 411 (2021).
(9) L. Li, Y. Guo, C. Zhao, and L. Song, *Macromol. Res.*, **26**, 592 (2018).
(10) A. Rasool, T. Z. Rizvi, S. Nayab, and Z. Iqbal, *J. Alloys Compd.*, **854**, 156661 (2021).
(11) Z. Zhou and J. Sun, *J. Phys. Conference Series*, **1790**, 012070 (2021).
(12) C. Wu, J. Wang, S. Song, Z. Wang, and S. Zhao, *Prog. Org. Coat.*, **148**, 105888 (2020).
(13) E. da C. Severo, V. S. F. Ederson Rossi Abaide, Chayene Gonçalves Anchieta, T. B. G., Caroline Trevisan Weber, G. C. Collazzoa, and E. L. F., Marcio Antonio Mazutti, *Mater. Res.*, **19**, 781 (2016).
(14) H. Y. Jeong, H. S. Lim, J. H. Lee, J. Heo, H. N. Kim, and S. O. Cho, *Nanomaterials*, **10**, 1 (2020).
(15) M. Li, X. Wang, Q. Zhu, J. G. Li, and B. N. Kim, *CrystEngComm*, **22**, 6398 (2020).
(16) R. Li, H. Lin, P. Lan, J. Gao, Y. Huang, Y. Wen, and W. Yang, *Polymers*, **10**, (2018).
(17) P. Raju, J. Shankar, J. Anjaiah, C. Kalyani, and G. Neeraja Rani, *J. Phys. Conference Series*, **1495**, (2020).
(18) L. Xu, X. Wang, M. L. Xu, B. Liu, X. F. Wang, S. H. Wang, and T. Sun, *Ultrason. Sonochem.*, **61**, 104815 (2020).
(19) M. M. Solomon, H. Gerengi, T. Kaya, and S. A. Umoren, *ACS Sustain. Chem. Eng.*, **5**, 809 (2016).
(20) N. Raghavendra, *Chem. Africa*, **2**, 463 (2019).
(21) N. Raghavendra and J. Ishwara Bhat, *Measurement*, **135**, 625 (2018).
(22) N. Raghavendra and J. Ishwara Bhat, *J. Bio- Tribo-Corrosion*, **4**, (2018).
(23) G. Harichandran, P. Divya, J. Yesuraj, and B. Muthuraaman, *Mater. Charact.*, **167**, 110490 (2020).
(24) M. Faisal and S. Khasim, *Polym. Sci. Series A*, **56**, 366 (2014).
(25) M. Faisal and S. Khasim, *Iranian Polym. J. (English Edition)*, **22**, 473 (2013).
(26) N. Maruthi, M. Faisal, N. Raghavendra, B. P. Prasanna, S. Manohara, and M. Revanasiddappa, *Synth. Met.*, **275**, 116744 (2021).
(27) J. Sun, L. Wang, Q. Yang, Y. Shen, and X. Zhang, *Prog. Org. Coat.*, **141**, 105552 (2020).
(28) K. Cheng, H. Li, M. Zhu, H. Qiu, and J. Yang, *RSC Adv.*, **10**, 2368 (2020).
(29) S. Lin, H. Wang, F. Wu, Q. Wang, X. Bai, D. Zu, J. Song, D. Wang, Z. Liu, Z. Li, N. Tao, K. Huang, M. Lei, B. Li, and H. Wu, *Npj. Flexible. Electronics*, **3**, 1 (2019).

(30) ASTM Committee G-1 on Corrosion of Metals, *Standard Practice for Preparing, Cleaning, and Evaluating Corrosion Test Specimens*, ASTM International, G1-03 (Vol 03:02), 2003.
(31) C. K. Madhusudhan, K. Mahendra, N. Raghavendra, M. Revanasiddappa, and M. Faisal, *J. Mater. Sci. Mater. Electron.*, **33**, 1366 (2022).
(32) W. K. Yaseen, S. B. Marpu, T. D. Golden, and M. A. Omary, *Surf. Coat. Technol.*, **404**, 126444 (2020).
(33) N. Raghavendra and J. I. Bhat, *Periodica Polytechnica Chem. Eng.*, **62**, 351 (2018).
(34) Y. Li, M. Zhou, Z. Xia, Q. Gong, X. Liu, Y. Yang, and Q. Gao, *Colloids Surf. A: Physicochem. Eng. Asp.*, **602**, 125172 (2020).
(35) B. Chethan, H. G. Raj Prakash, Y. T. Ravikiran, S. C. Vijaya Kumari, S. Manjunatha, and S. Thomas, *Talanta* **215**, 120906 (2020).
(36) Y. Wang, L. Liping, and G. Li, *Appl. Surf. Sci.*, **393**, 159 (2017).
(37) G. Harichandran, P. Divya, J. Yesuraj, and B. Muthuraaman, *Mater. Charact.*, **167**, 110490 (2020).
(38) B. P. Prasanna, D. N. Avadhani, M. S. Raghu, and Y. Kumar, *Mater. Today Commun.*, **12**, 72 (2017).
(39) E. R. Abaide, C. T. Weber, T. B. Garlet, G. C. Collazzo, M. Antonio, R. C. Kuhn, and E. L. Foletto, *Mater. Res.*, **19**, 781 (2016).
(40) W. Wu, Z. Lin, H.-Y. Shi, L. Lin, X. Yang, Y. Song, X.-X. Liu, and X. Sun, *Chem. Eng. J.*, **427**, 131988 (2022).
(41) V. Wadalkar, G. Mishra, A. Kumar, P. Aishwarya, S. Kallol, and S. A. College, *Int. J. Sci. Res. Develop.*, **4**, 1039 (2016).
(42) Q. Ning, C. Zhou, and Y. Shi, *J. Mater. Sci., Mater. Electron.*, **31**, 10499 (2020).
(43) N. Maruthi, Muhammad Faisal, and N. Raghavendra, *Synth. Met.*, **272**, 116664 (2021).
(44) M. Faisal and S. Khasim, *J. Mater. Sci. Mater. Electron.*, **24**, 2202 (2013).
(45) Y. Yang, J. Zhu, W. Shi, J. Zhou, D. Gong, S. Gu, L. Wang, Z. Xu, and B. Lu, *Mater. Lett.*, **177**, 34 (2016).
(46) A. I. Ahmed, D. A. Kospa, S. Gamal, S. E. Samra, A. A. Salah, S. A. El-Hakam, and A. A. Ibrahim, *J. Photochem. Photobiol. A: Chem.*, **429**, 113907 (2022).
(47) R. D. Kumar, Y. Andou, and S. Karuppuchamy, *J. Phys. Chem. Solids*, **92**, 94 (2016).
(48) J. Yesuraj and S. A. Suthanthiraraj, *J. Molecular Structure* **1181**, 131 (2019).
(49) M. W. Kadi and R. M. Mohamed, *Front. Nanosci. Nanotechnol.*, **5**, 1 (2019).
(50) L. Sun, Y. Shi, Z. He, B. Li, and J. Liu, *Synthetic Metals* **162**, 2183 (2012).
(51) N. Maruthi, M. Faisal, N. Raghavendra, B. P. Prasanna, R. Manohara, and M. Revanasiddappa, *Colloids Surf. A: Physicochem. Eng. Asp.*, **621**, 126611 (2021).
(52) K. R. Nandan, L. S. Lobo, G. Murugesan, N. Maruthi, and A. Ruban Kumar, *J. Mater. Sci. Mater. Electron.*, **33**, 8355 (2022).
(53) S. Varshney, A. Ohlan, V. K. Jain, V. P. Dutta, and S. K. Dhawan, *Mater. Chem. Phys.*, **143**, 806 (2014).
(54) N. Maruthi, M. Faisal, N. Raghavendra, B. P. Prasanna, K. R. Nandan, K. Y. Kumar, and S. B. B. Prasad, *Mater. Chem. Phys.*, **259**, 124059 (2021).
(55) C. K. Madhusudhan, K. Mahendra, B. S. Madhukar, T. E. Somesh, and M. Faisal, *Polym. Sci. Series B*, **63**, 280 (2021).
(56) C. K. Madhusudhan, K. Mahendra, B. S. Madhukar, T. E. Somesh, and M. Faisal, *Synth. Met.*, **267**, 116450 (2020).
(57) K. Zhang, W. Yang, X. Yin, Y. Chen, Y. Liu, J. Le, and B. Xu, *Carbohydr. Polym.*, **181**, 191 (2018).

